

On CD-AFM bias related to probe bending

V.A. Ukraintsev^{*a,b,c}, N.G. Orji^a, T.V. Vorburger^a, R.G. Dixon^a, J. Fu^a, and R.M. Silver^a

^aSemiconductor and Dimensional Metrology Division, National Institute for Standards and Technology, & Gaithersburg, Maryland, USA

^bInstitute for Research in Electronics and Applied Physics, University of Maryland, USA

^cNanometrology International, Inc., Allen, Texas, USA

ABSTRACT

Critical Dimension AFM (CD-AFM) is a widely used reference metrology. To characterize modern semiconductor devices, very small and flexible probes, often 15 nm to 20 nm in diameter, are now frequently used. Several recent publications have reported on uncontrolled and significant probe-to-probe bias variation during linewidth and sidewall angle measurements [1,2]. Results obtained in this work suggest that probe bending can be on the order of several nanometers and thus potentially can explain much of the observed CD-AFM probe-to-probe bias variation. We have developed and experimentally tested one-dimensional (1D) and two-dimensional (2D) models to describe the bending of cylindrical probes. An earlier 1D bending model reported by Watanabe *et al.* [3] was refined. Contributions from several new phenomena were considered, including: probe misalignment, diameter variation near the carbon nanotube tip (CNT) apex, probe bending before snapping, distributed van der Waals-London force, etc. The methodology for extraction of the Hamaker probe-surface interaction energy from experimental probe bending data was developed. To overcome limitations of the 1D model, a new 2D distributed force (DF) model was developed. Comparison of the new model with the 1D single point force (SPF) model revealed about 27 % difference in probe bending bias between the two. A simple linear relation between biases predicted by the 1D SPF and 2D DF models was found. This finding simplifies use of the advanced 2D DF model of probe bending in various CD-AFM applications. New 2D and three-dimensional (3D) CD-AFM data analysis software is needed to take full advantage of the new bias correction modeling capabilities.

Keywords: CD-AFM, reference metrology, accuracy, measurement bias, probe bending, van der Waals-London, CNT

NOTATION

a	Radius of cylindrical probe [m]
A	Isotropic Hamaker coefficient [J]
β	Probe bending model constant [$\text{m}^{5/7}$]
δ	The Dirac function
E	Elastic modulus [Pa]
f	van der Waals-London force [N]
f_{tg}	van der Waals-London force at the snapping point [N]
F	Total force acting on probe [N]
g	van der Waals-London energy per unit length [J/m]
G	Total energy of probe-sample system [J]
$G_{elastic}$	Elastic energy of bended probe [J]
I	Second moment of area of the probe [m^4]
ℓ	Sample to probe gap [m]
$\Delta\ell$	Probe bending before the snapping point [m]
ℓ_{tg}	Sample to probe gap at the snapping point [m]

* ukrainsev@nanometrology.net; phone 1 469 854-1579; fax 1 469 854 3561; nanometrology.net

& Official contributions of the National Institute of Standards and Technology are not subject to copyright in the United States.

ℓ_{total}	Total probe bending [m]
ℓ_{DF}	Total probe bending calculated using DF model [m]
ℓ_{SPF}	Total probe bending calculated using SPF model [m]
L	Probe length [m]
LW	Dilated linewidth of Improved Vertical Parallel Structure (IVPS) [m]
k_e	Effective flexural spring constant of probe-cantilever system [N/m]
k_p	Probe flexural spring constant [N/m]
k_t	Torsional spring constant of cantilever [N/m]
q	Force per probe unit length [N/m]
R	Ratio of ω to ℓ_{total}
R_{CNT}	Radius of curvature of CNT probe [m]
R_{IVPS}	Radius of curvature of the IVPS [m]
R_{top}	Radius of curvature of dilated IVPS image [m]
Θ	The unit step function
ω	Probe bending [m]
ω_{DF}	Probe bending calculated using DF model [m]
ω_{SPF}	Probe bending calculated using SPF model [m]
W	Ratio of Z to L
Z	Sample to probe overlap [m]
Z_1	Lower overlap used to estimate β [m]
Z_2	Higher overlap used to estimate β [m]
Z_T	Z -scale shift to compensate for transient effects [m]

1. INTRODUCTION

Critical dimension AFM (CD-AFM) is one of a few reference metrology techniques used by the semiconductor industry today. To measure the critical dimensions (CD) of modern devices, very small and flexible probes, often 15 nm to 20 nm in diameter, are now commonly used. There is a growing demand even for smaller probes in the diameter range of 5 nm to 10 nm. Several recent publications have reported on uncontrolled and significant probe-to-probe CD-AFM bias variation during linewidth and sidewall angle measurements [1,2]. In previous work, Watanabe et al. reported results suggesting that the bending of a cylindrical probe of 20 nm to 30 nm diameter could be on the order of several nanometers [3]. Therefore, it is important to understand and assess the impact of the probe bending on the calibration of probe width and thus the accuracy of CD-AFM linewidth and sidewall angle measurements. In Sections 2 and 3 of this paper, we develop refinements and show experimental tests of the 1D single point force (SPF) bending model originally developed by Watanabe *et al.* [3]. Contributions from several new phenomena are considered. The methodology for extraction of the Hamaker probe-surface interaction energy from experimental probe bending data is described in Section 4. To overcome the limitations of the 1D model, a new 2D distributed force (DF) model was developed and is described in Sections 5 and 6. In the conclusion, we discuss some potential applications of the new CD-AFM bias correction modeling capabilities that we have developed.

2. CYLINDRICAL PROBE BENDING MODEL

According to Rajter *et al.* [4] the van der Waals-London (vdW-Ld) interaction energy per unit length between a cylinder of radius a and an isotropic plane is given by:

$$g(l, a) = -\frac{\sqrt{2aA}}{24l^{3/2}}, \quad (1)$$

where l is the size of the uniform gap (distance) between the plane and the cylinder, and A is the isotropic Hamaker coefficient, respectively.

The corresponding force between a cylindrical probe of length Z and a sidewall is then (Fig. 1):

$$f(l, a) = \frac{\sqrt{2aAZ}}{16l^{5/2}}. \quad (2)$$

This equation compares with Eq. 11 in the paper by Watanabe *et al.* [3], but it has proper units of force. For further treatment of the vdW-Ld force in this paper, we will use our Eq. 2.

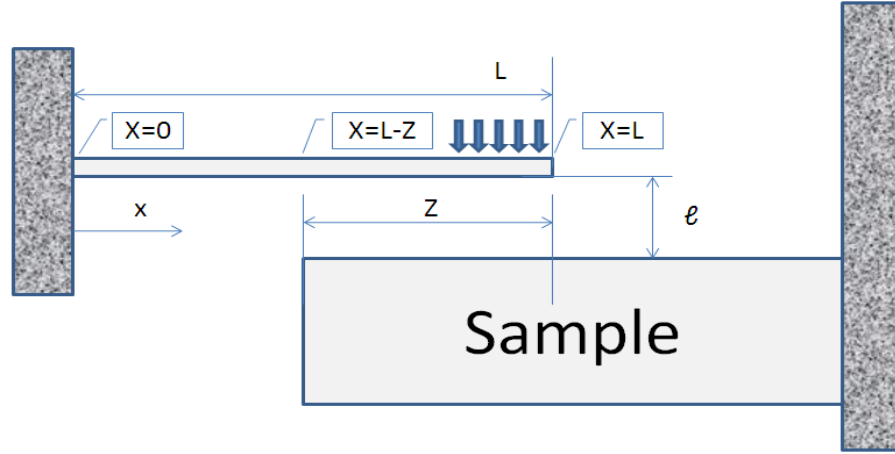


Figure 1. Probe of the total length L with partial overlap Z with the sample.

The probe will snap to the wall at a distance l_{tg} where the first derivatives of the vdW-Ld force and the effective flexural spring constant of the probe-cantilever system relative to a lumped load at the apex of the probe are equal [3,5]:

$$k_e = \frac{5\sqrt{2aAZ}}{32l_{tg}^{7/2}}. \quad (3)$$

The force at l_{tg} is given by:

$$f_{tg}(l_{tg}, a) = \frac{\sqrt{2aAZ}}{16l_{tg}^{5/2}} = k_e \Delta l, \quad (4)$$

where the Δl is the probe bending before the snapping point l_{tg} is reached.

Therefore, for $l_{total} = l_{tg} + \Delta l$ one gets:

$$l_{total} = \frac{7}{5} \left(\frac{5\sqrt{2aAZ}}{32k_e} \right)^{2/7}. \quad (5)$$

Using Eq. 5 for the Hamaker coefficient one has:

$$A = \frac{32k_e \left(\frac{5l_{total}}{7} \right)^{3.5}}{5\sqrt{2aZ}}. \quad (6)$$

The effective flexural spring constant of the probe-cantilever system k_e is [3]:

$$k_e = \frac{k_p k_t}{k_p + k_t}, \quad (7)$$

where k_p and k_t are the torsional spring constants for probe and cantilever, respectively.

The probe flexural spring constant k_p can be calculated using the following equation:

$$k_p = \frac{3\pi E a^4}{4L^3}, \quad (8)$$

where E is the CNT's elastic modulus ($E = 1$ TPa [3]).

Therefore, for the probe used by Watanabe *et al.* ($L = 220$ nm, $a = 12$ nm) one obtains $k_p = 4.6$ N/m. Using Watanabe's probe $k_t = 110$ N/m we have $k_e = 4.4$ N/m. Then for the Hamaker coefficient (Eq. 6) for $Z = 100$ nm and $l_{total} = 6.7$ nm [3] an unreasonably high value of $A \approx 86$ eV is obtained. Typical values for the Hamaker coefficient are about 0.03 eV to 4 eV [6]. We thus see a significant discrepancy between the model [3] expectation and experimental data. To investigate the causes of this discrepancy, we tried to reproduce the experiment—as described in the next section.

3. EXPERIMENTAL OBSERVATIONS FOR CNT500 PROBES

In our experiment, we use multiwall CNT500 probes manufactured by Sumitomo/Daiken Chemical[†]. The probes were characterized using an Improved Vertical Parallel Structure (IVPS) [7]. Measurements were done using the Bruker “deep trench” (DT) mode of scanning. Six average profiles (each an average of 20 line scans taken along the IVPS) were obtained for CNT500 (P1), and these are shown overlaid in Fig. 2. These are raw images, which include tip dilation, and the probe shape is not extracted (eroded). Clamping of the z -axis travel down the trench was set at 500 nm. Therefore, the probe did not reach the bottom of the 1000 nm deep IVPS structure.

The data (Fig. 2) show that the top corners are rounded with $R_{TOP} \approx 20$ nm. The radius is a sum of R_{IVPS} and R_{CNT} . R_{IVPS} is expected to be in the range of 2 nm to 5 nm [8]. R_{CNT} should be close to $\frac{1}{2}$ of the tip width (TW) and is expected to be approximately 15 nm to 20 nm. It is important to realize that for $Z < 20$ nm the interaction between the CNT and the wall is not at full strength yet. Therefore, we suggest a shift of the Z scale by $Z_T \approx R_{TOP}$ to compensate for the effect. In the following modeling of CNT500 bending (Section 4) we will consider Z_T in the range of 0 nm to 30 nm.

As clearly seen in Fig. 2 the dilated profile of the IVPS has non-vertical sidewalls. This AFM artifact has been explained by Watanabe *et al.* [3]. As expected from the probe bending model (Eq.5, Fig. 3), the bending error l_{total} grows quickly for the first 200 nm of Z and then continues its growth at a lower rate.

As was experimentally observed by Watanabe *et al.*, in the proximity of a sharp corner, the AFM probe bends toward and slips into the trench producing an artifact of early rounding of the corner. According to the probe slipping model developed by Morimoto *et al.* [9] for a CNT500 with $k_p \approx 1$ N/m, corner angle of 90° , and probe force of 1 nN, one should expect slipping of about 1 nm. Fig. 3 shows examples of slipping (negative bending values at low vertical distance) observed for CNT500 (P1) and (P3) probes.

The IVPS structure should have vertical sidewalls formed by crystallographically selective etching of c-Si. The sidewall angle (SWA) of the IVPS structure is 89.95° as measured using a flared CDR50 probe and CD-AFM scanning mode. In

[†] Certain commercial equipment is identified in this paper to adequately describe the experimental procedure. Such identification does not imply recommendation or endorsement by the National Institute of Standards and Technology nor does it imply that the equipment identified is necessarily the best available for the purpose.

the following modeling of CNT500 bending, we neglect the minor deviation of the measured SWA from 90° and assume that the IVPS structure has absolutely vertical sidewalls. This could potentially cause an error of about 0.4 nm which is comparable with uncertainty of CD-AFM for this type of measurement.

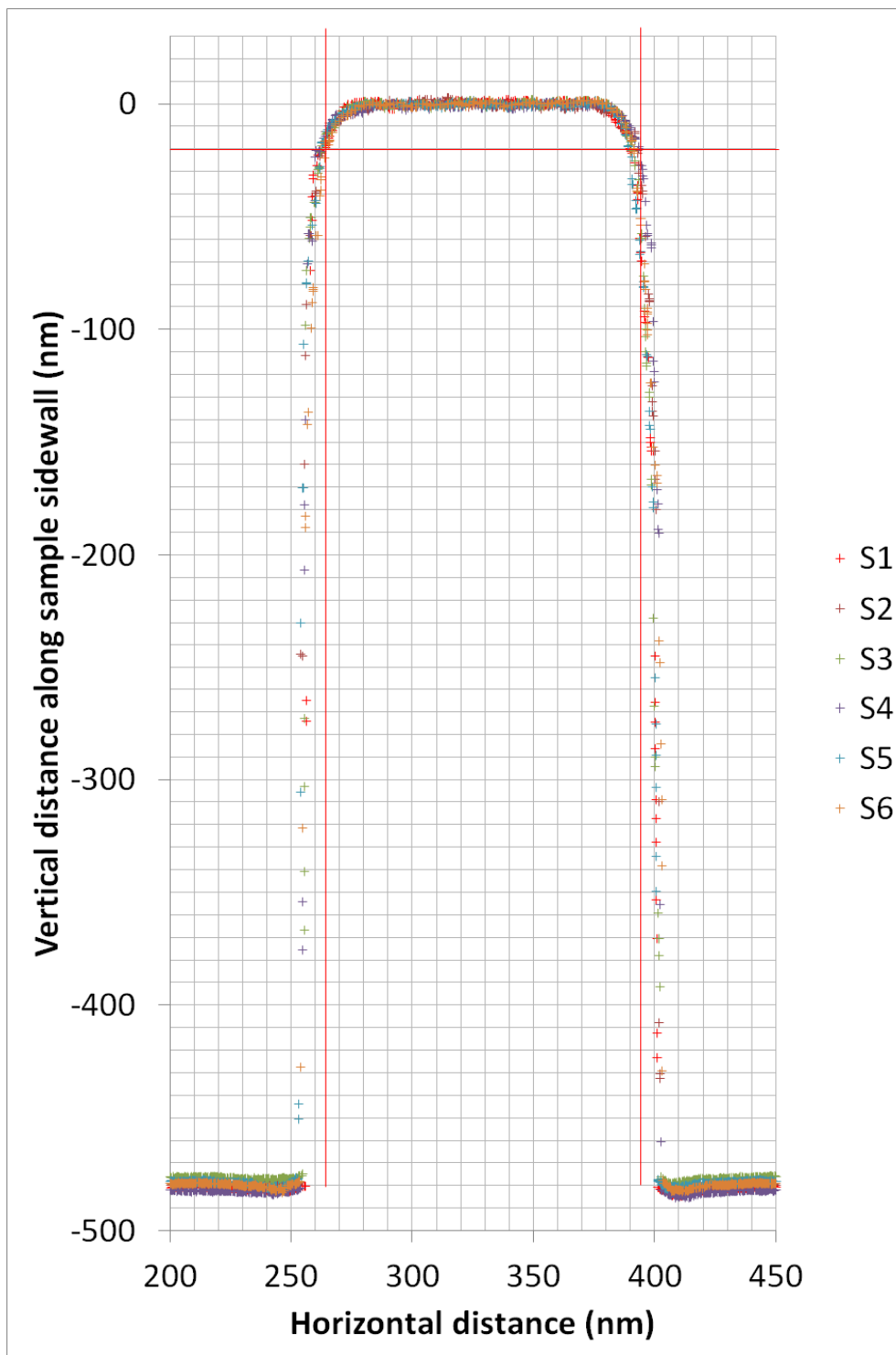


Figure 2. Six overlaid dilated profiles of an IVPS obtained in DT mode using a CNT500 (P1) probe.

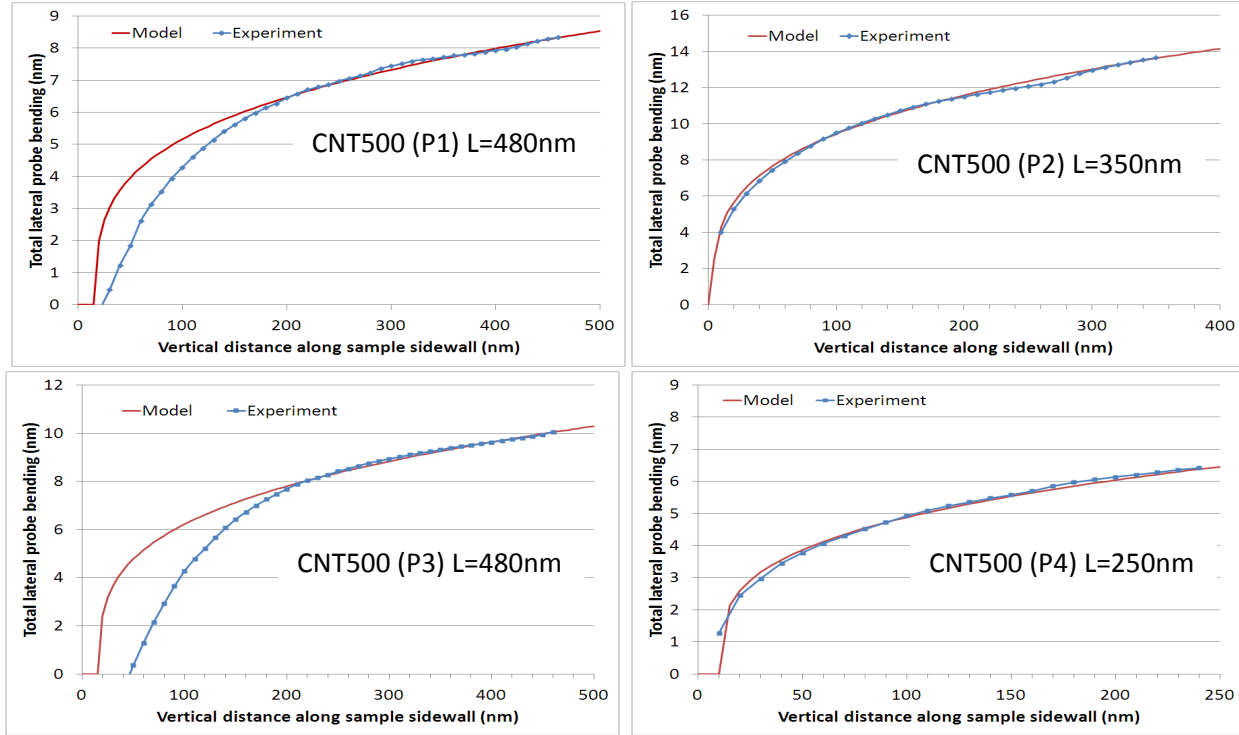


Figure 3. Variation of lateral CNT500 bending with increasing depth (Z in Eq. 5) of the probe along the IVPS sidewall. Probe CNT500 (P1) data (top-left) are extracted from Fig. 2. Probe CNT500 (P2) has reduced length of 350 nm top-right). Probe CNT500 (P3) has original length of 480 nm (low-left). Probe CNT500 (P4) has reduced length of 250 nm (low-right). Model is described in Section 4.

4. MODELING OF EXPERIMENTAL CNT PROBE BENDING DATA

In this section we model CNT500 bending using Eqs. 5-8. In our experiment we use a cantilever with $k_t = 1400$ N/m. Therefore, for $k_t \gg k_p$ one gets $k_e \cong k_p$ and the probe bending error (l_{total}) can be expressed in the following relatively simple form:

$$l_{total}(Z) \cong \frac{0.7}{a} \left(\frac{10AZL^3}{3\pi E} \right)^{2/7} \cong \frac{0.7L}{a} \left(\frac{AZ}{E\sqrt{L}} \right)^{2/7}. \quad (9)$$

Further we introduce a Z scale shift or Z_T as discussed in Section 3:

$$l_{SPF}(Z) \cong \frac{0.7L}{a} \left(\frac{A(Z-Z_T)}{E\sqrt{L}} \right)^{2/7}. \quad (10)$$

Equation 11 can be presented in a different form:

$$l_{SPF}(Z) = \beta (Z - Z_T)^{2/7}, \quad (11)$$

where

$$\beta \cong \frac{0.7L}{a} \left(\frac{A}{E\sqrt{L}} \right)^{2/7}. \quad (12)$$

One can quite accurately estimate β using the IVPS linewidth measurements taken at two different heights (Fig. 1). Difference between these two measurements can be expressed as:

$$LW(Z_1) - LW(Z_2) = 2(l_{SPF}(Z_1) - l_{SPF}(Z_2)) = 2\beta \left[(Z_1 - Z_T)^{2/7} - (Z_2 - Z_T)^{2/7} \right]$$

or

$$\beta = \frac{LW(Z_1) - LW(Z_2)}{2 \left[(Z_1 - Z_T)^{2/7} - (Z_2 - Z_T)^{2/7} \right]} \quad (13)$$

Since various factors (see Section 2) may impact $l_{SPF}(Z)$ at small Z , we used larger Z_1 and Z_2 for this procedure. For CNT500 (P1) we used $Z_1 = 240$ nm and $Z_2 = 460$ nm (Fig. 1). The IVPS linewidth difference between the two measurements is 2.95 nm \pm 0.24 nm, where the expanded uncertainty is estimated using a coverage factor of $k = 2$. Assuming $Z_T = 17$ nm, the estimated value of β is $5.4 \times 10^{-7} \text{ m}^{5/7} \pm 0.4 \times 10^{-7} \text{ m}^{5/7}$ ($k = 2$). Once β is known, probe bending at any Z can be readily estimated using Eq. 11. Again, the most accurate $l_{SPF}(Z)$ estimations should occur for larger differences between Z_1 and Z_2 . CNT500 bending at $Z = 460$ nm is 8.3 nm. Since the linewidth of the IVPS is calibrated using a SI-traceable NanoCD standard [10], the effective (or observed) TW at depth 460 nm is estimated at 52.3 nm \pm 0.9 nm ($k = 2$). Once the effective $TW(Z)$ and $l_{SPF}(Z)$ are known, the radius of the CNT can be estimated from $a = 0.5 \times TW(Z) - l_{SPF}(Z) = 0.5 \times (52.3 - 16.6) = 17.9$ nm.

Equation (12) can be used to estimate the A/E ratio:

$$\frac{A}{E} \cong \sqrt{L} \left(\frac{a\beta}{0.7L} \right)^{7/2} \quad (14)$$

Using $\beta = 5.44 \times 10^{-7} \text{ m}^{5/7}$, $L = 500$ nm, and $a = 17.9$ nm one gets $A/E \cong 1.26 \times 10^{-30} \text{ m}^3$.

Assuming $E = 0.5$ TPa (measured for multiwall CNT by Akita et al. [11,12]), one gets a rather large value for $A = 3.95$ eV. The large value of the measured Hamaker coefficient of CNT is not yet well understood. We speculate that the probe lateral noise and induced vertical oscillations, capillary effects, and electrostatic forces may contribute to the stronger apparent attraction of the CNT probe to the surface. This speculation needs to be further investigated.

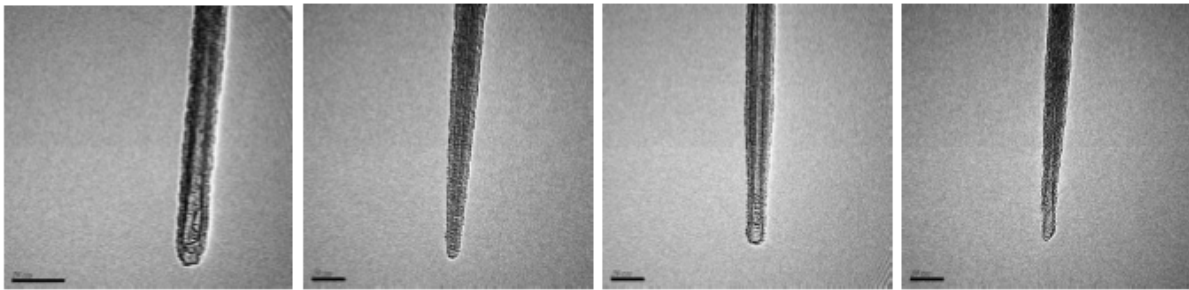


Figure 4. TEM images of CNT probes. Courtesy of Sumitomo and Daiken Chemical Corporation [13].

In our estimations we use the experimental (rather than the theoretical $E = 1$ TPa) value for CNT elastic modulus. According to Tanigaki *et al.* [14] CNT could be covered by a thin layer of amorphous carbon or other material formed during cooling of the freshly formed CNT. High-resolution TEM images show that a 3 nm to 4 nm thick layer of amorphous carbon is covering certain CNT probes. This layer would increase the TW of CNT (measured by AFM) and might cause overestimation of its spring constant. We try to minimize this potential error by using an experimentally

measured value of Young's modulus for a multiwall CNT similar to our probe [11]. The experimentally measured value of Young's modulus for a multiwall CNT with diameter of 26 nm is only half of the theoretically predicted value of 1 TPa. This is in agreement with Eq. 8 which suggests that the 22 nm diameter 1 TPa probe should have the same spring constant as a 26 nm diameter 0.5 TPa probe.

Measurements of probe bending were done for three other multiwall CNT probes. Experimental results and model fits are shown in Fig 3. Probes of original length P1 and P3 clearly show discrepancies between experimental and modeled data for Z values below 200 nm. However, probes of reduced length, P2 and P4, show good matches between experimental and modeled results. This observation may suggest that, depending on how the apex of the CNT probe is formed (cut), its diameter may vary near the apex. To verify this idea we reviewed several high-resolution TEM images of CNT probes found in the literature and also provided by Daiken Chemical Corporation. We found that for CNT probes, which are truncated using a DC arc discharge, a noticeable diameter reduction near the apex is often observed. Fig. 4 shows examples of CNT diameter variation near probe apex. Our data suggest that mechanically truncated (broken or worn) CNTs (P2 and P4) are more likely to have less diameter variation near their apices.

Let us summarize revisions made to the 1D SPF cylindrical probe bending model [3]:

1. Exponent of $l_{SPF}(Z)$ dependence: $l_{SPF}(Z) \sim Z^{2/7}$ (cf. Eq. 5 to Eq. 15 of [3])
2. Total probe bending distance is $1.4 \times$ snapping distance: $l_{SPF}(Z) = 1.4l_{tg}(Z)$ (cf. Eq. 15 of [3])
3. Effective Z is reduced by Z_T : $l_{SPF}(Z) \sim (Z - Z_T)^{2/7}$ (cf. Eq. 10 to Eq. 15 of [3])
4. Experimental and model data mismatch at small Z is likely related to CNT diameter variation near apex. This was often observed for CNT truncated using DC discharge.

The changes in the model brought the estimated Hamaker coefficient for CNT/Si interaction into a reasonable proximity with other experimental results and with theoretical expectations. Estimated A values are: 3.95 eV (P1), 1.40 eV (P2), 6.12 eV (P3), and 3.48 eV (P4). The theoretical A value for CNT/CNT interaction is about 0.9 eV [4]. The experimental A value for CNT/Os interaction is 3.75 eV [12].

5. MODELING OF PROBE BENDING FOR DISTRIBUTED vdW-LD FORCE

The good sub-nanometer agreement between experimental data and model is encouraging (Fig. 3). However, the developed model is based on questionable assumptions. First, following Watanabe *et al.* [3] we assumed that the vdW-Ld force is applied to the very end of the probe (Eqs. 3-5). This is not correct since the attractive vdW-Ld force is distributed along the Z portion of the probe. Second, to simplify the calculation of the total vdW-Ld force acting on the probe, it is assumed that the probe is parallel to the surface and that the probe-sample gap l is not changing along the probe length (Eq. 2). Therefore, the SPF model described in Sections 2 and 4 is only a basic approximation of the process, and the accuracy of extracted physical values should be verified.

A more accurate model can be found using Euler-Bernoulli beam theory [15, 16]. The Euler-Bernoulli equation describes a beam's deflection (bending) as a function of the applied load:

$$\frac{d^2}{dx^2} \left(EI \frac{d^2 \omega}{dx^2} \right) = q(x), \quad (15)$$

where the $\omega(x)$ is bending (deflection), E is Young's modulus or elasticity modulus, $I(x)$ is the second moment of the area of the beam, and $q(x)$ is the load (force) distributed along the beam. If the product $EI(x)$ is a constant (which is true for cylindrical but not conical or flared probes), the Euler-Bernoulli equation can be simplified to:

$$EI \frac{d^4 \omega}{dx^4} = q(x). \quad (16)$$

The 1D SPF bending data can be obtained using the following equation:

$$EI \frac{d^4 \omega}{dx^4} = f \delta(x - L), \quad (17)$$

where $f = \frac{\sqrt{2aAZ}}{16l_{tg}^{2.5}}$ and l_{tg} are defined by Eqs. 2-3 and $\delta(x)$ is the Dirac function.

The boundary conditions are:

$$\begin{aligned} (1) \quad & \omega(0) = 0 \\ (2) \quad & \omega'(0) = 0 \\ (3) \quad & \omega''(L) = 0 \\ (4) \quad & \omega'''(L+) = 0. \end{aligned} \quad (18)$$

$L+$ refers to the limit $x \rightarrow L$ from above. Equations 17-18 can be solved analytically, and the bending function $\omega(x)$ is:

$$\omega(x) = \frac{fx^2(3L-x)}{6EI} \quad (19)$$

or

$$\omega(x) = \frac{\omega(L)x^2(3L-x)}{2L^3}. \quad (20)$$

In the more general case of a variable distributed vdW-Ld force, $q(x)$ is similar to Eq. 2:

$$q(x) = -\frac{\sqrt{2aA}}{16l(x)^{5/2}} = -\frac{\sqrt{2aA}}{16[l_{DF}-\omega(x)]^{5/2}}, \quad (21)$$

where l_{DF} is the probe-sample gap for zero beam deflection (*cf.* l_{total} of Eq. 5).

Using Eqs. 16 and 21 for a cylindrical probe ($I = \pi a^4/4$) one gets:

$$\frac{d^4 l(x)}{dx^4} = \frac{\sqrt{2aA}}{4\pi E a^4 l(x)^{5/2}}. \quad (22)$$

If the probe is only partially overlapping with the IVPS structure (Fig. 1) then one would have to solve the following differential equation with four boundary conditions:

$$\frac{d^4 l(x)}{dx^4} = \frac{\sqrt{2aA}\theta(x-L+Z)}{4\pi E a^4 l(x)^{5/2}}, \quad (23)$$

where $\theta(x)$ is the unit step function defined as $\theta(x) = 1$ for $x \geq 0$ and $\theta(x) = 0$ for $x < 0$.

The boundary conditions are:

$$\begin{aligned} (1) \quad & l(0) = l_{DF} \\ (2) \quad & l'(0) = 0 \\ (3) \quad & l''(L) = 0 \\ (4) \quad & l'''(L) = 0. \end{aligned} \quad (24)$$

Solving this differential equation analytically is not a trivial task. Therefore, we utilize numerical methods to solve the equation. First, we compare probe bending for the force calculated using Eq. 2 and apply to the probe apex (SPF) a high accuracy numerical solution obtained using Eqs. 23 and 24. Calculations are done for a CNT probe with 480 nm length and 15 nm radius. The probe was placed at $l_{DF} = 6.7$ nm from the IVPS wall with an overlap $Z = 240$ nm. A Hamaker coefficient A of 3.95 eV was used in the calculations. We observed a significant difference (factor of 3) between the approximate 1D SPF (larger bending) and high accuracy numerical (smaller bending) solutions.

6. MODELING OF PROBE SNAPPING FOR DISTRIBUTED vdW-LD FORCE

The 1D SPF model predicts probe snapping for $l_{total} = 6.7$ nm and $Z = 240$ nm (the case discussed at the end of Section 5). Probe snapping was defined in the 1D SPF model by Eqs. 3 and 4, which work within the approximation discussed above—probe parallelism with the sidewall—and for a mechanical system with invariable spring constant Eqs. 7-8 (i.e., the force is applied to probe's apex). But how is the probe snapping condition defined in the new 2D distributed force model? Could a similar probe snapping model be developed for a variable distributed vdW-Ld force? To do that one could use an approach proposed by Meyer *et al.* [17,18] and further developed by Sarid [19]. Within this approach the total energy of the probe-sample system E has to be defined as a function of the probe bending ω , the probe-sample distance before bending l_{DF} , and the probe-sidewall overlap Z . Once the system energy is known, the total force $\frac{dG(\omega)}{d\omega} = -F(\omega)$ acting on the probe in the lateral direction can be calculated. Within certain ranges of l_{DF} and Z , the total energy of the system has two minima ($F = 0$) separated by an energy barrier. The transition between these two total energy minima is defined as the probe snapping. As Z grows larger, the barrier decreases/ and at a certain critical Z value it disappears meaning that the force would never become repulsive until the second minimum, the one closer to the surface, is reached. This approach was developed for the simpler 1D case of vertical snapping of an AFM probe where the point interaction and invariable spring constant are good approximations for the model [17-19]. The modeling becomes more complex for the 2D variable sample-probe gap and distributed lateral force.

The solution for a distributed lateral force is complex since probe bending can be calculated using numerical methods only. The case is further complicated since numerical methods fail near the unstable snapping point. Figure 5 shows the results of numerical calculations for the system described in Section 5. As the gap l_0 between the probe and sidewall decreases, the probe apex bending $\omega(L)$ increases until it reaches an unstable “snapping” point (≈ 2 nm bending and gap $l_{DF} = 5.4$ nm). Beyond this point the numerical solution becomes erroneous and the bending decreases despite further reduction of the gap, an unphysical result. At this “snapping” point the numerically calculated value of $\frac{dF(l_{DF},Z)}{d\omega(L)}$ approaches zero as expected in accord with the Meyer-Sarid model of snapping [17-19].

Similar numerical calculations were performed for series of Z values from $Z = 0$ to $Z = L$. For each Z point, the total probe bending l_{DF} at the “snapping” point was determined. As expected, the numerical DF model predicts a smaller probe bending error l_{total} than the SPF model. For $Z = L$ the 1D SPF model overestimates the total probe bending by 46 % (Fig. 7). As Z approaches 0, both models yield similar results. This is expected since the SPF model approximation (single point force and uniform probe-sample force) becomes accurate with Z near 0. However, as was mentioned before, the numerical model yields unphysical results for cases beyond the “snapping” point (Fig. 5, probe-sample gap less than 5.4 nm). What then is the accuracy of the numerical solution near the snapping point? This question could be answered if an analytical solution for the distributed force case is found.

6.1 Distributed force snapping model using SPF probe bending approximation

To verify the numerical DF model solution, one may use the SPF probe bending approximation. The approximation is based on the observation of a close (sub 0.1 nm) agreement between the probe shapes for DF and SPF bending (Fig. 6).

The data in Fig. 6 suggest that for any probe-sample gap l_0 and overlap Z an exact probe shape $\omega_{DF}(x)$, numerically calculated for the DF case, is closely approximated by the simple analytical SPF expression $\omega_{SPF}(x)$ (Eq. 20) - under the condition that $\omega_{DF}(L) = \omega_{SPF}(L)$.

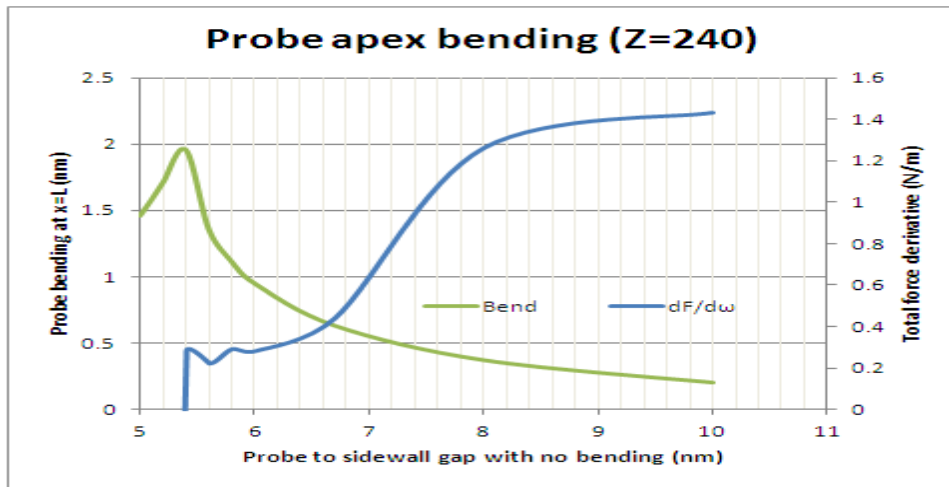


Figure 5. Numerically calculated probe bending $\omega(L)$ and $dF/d\omega$ at $x = L$ vs. the sidewall-probe gap for a 480 nm long CNT probe with $a = 15$ nm, $E = 0.5$ TPa, $A = 3.95$ eV, and $Z = 240$ nm.

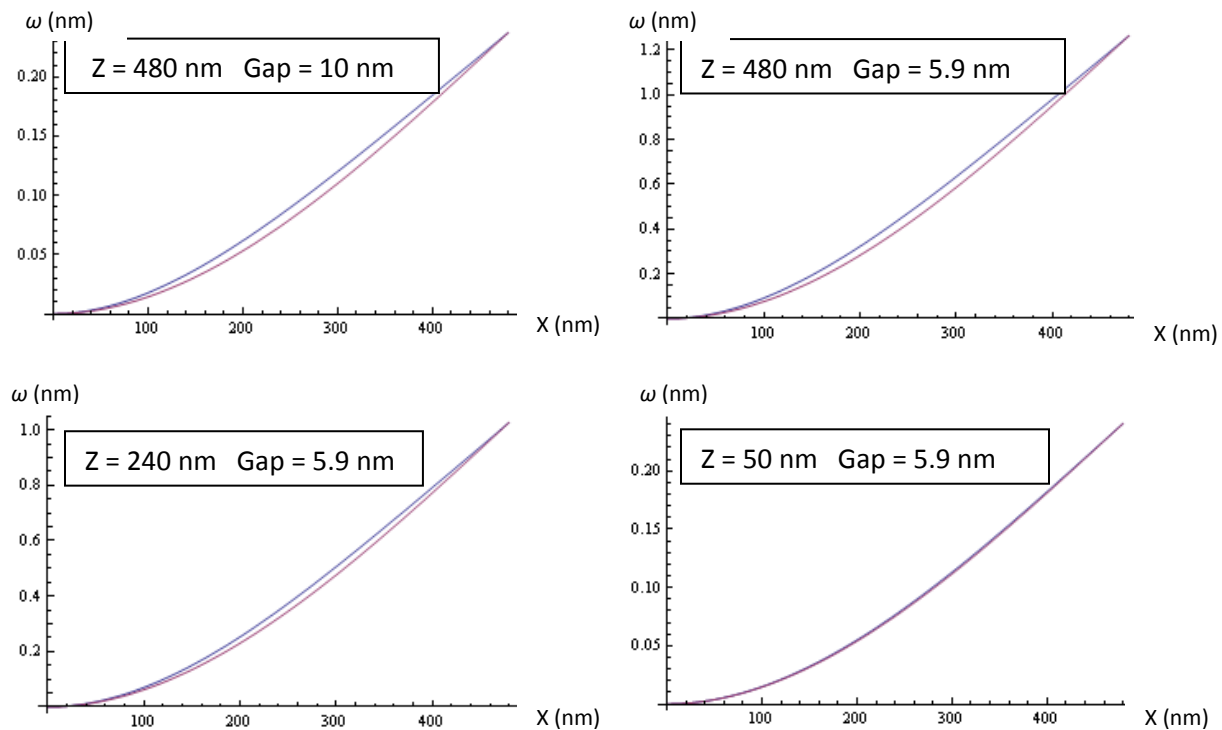


Figure 6. Comparison of probe shape $\omega(x)$ for DF and SPF bending models when total bending is the same. The plots show that, for various values of sample-probe overlap Z and gap l_{DF} , the numerically calculated probe shape for DF $\omega_{DF}(x)$ is closely approximated by the analytical expression for SPF probe shape $\omega_{SPF}(x)$ (Eq. 20), with the constraint that $\omega_{DF}(L) = \omega_{SPF}(L)$. The calculations are done for a 480 nm long CNT probe with $a = 15$ nm, $E = 0.5$ TPa, and $A = 3.95$ eV.

Therefore, to calculate the total system energy for distributed lateral vdW-Ld force one may use the SPF approximation. Then for the elastic energy of the bending probe and its shape one gets

$$G_{elastic} \cong \frac{1}{2} k_e \omega_{DF}^2(L) \quad (25)$$

and

$$\omega_{DF}(x) = \frac{\omega_{DF}(L)x^2(3L-x)}{2L^3}. \quad (26)$$

Within the SPF approximation the distance between probe and sample along the probe can be expressed symbolically, and, therefore, the vdW-Ld force, the elastic energy, and the total energy of the system can be calculated analytically (cf. Eq. 1):

$$G(l_{DF}, Z) \cong - \int_{L-Z}^L \frac{\sqrt{2a}Adx}{24[l_{DF}-\omega(x)]^{3/2}} + \frac{1}{2} k_e \omega^2(L). \quad (27)$$

Using Eq. 27 we calculate total force acting on the probe's apex as [20]:

$$F(l_{DF}, Z)|_{x=L} = \frac{\sqrt{2a}AL}{36[l_{DF}-\omega(L)]^{3/2}\omega(L)} - \frac{\sqrt{2a}AL}{36[l_{DF}-\omega(L-Z)]^{3/2}\omega(L)} - k_e \omega(L). \quad (28)$$

Using the snapping conditions ($F = 0$ and $dF/d\omega = 0$) and Eq. 28, one can calculate $\omega(L)/l_{DF}$ ratio for every $W = Z/L$ ($0 \leq W \leq 1$) value (Table 1).

Table 1. Dependence of $\omega(L)$ to l_{DF} ratio on Z/L ratio [20].

W=Z/L	1	0.9	0.8	0.7	0.6	0.5	0.4	0.3	0.2	0.1	0.05	0.03	0.01	0.00001
R= ω/l_{DF}	0.321	0.321	0.320	0.318	0.315	0.312	0.307	0.303	0.297	0.292	0.289	0.288	0.286	0.286

Knowing $R = \omega/l_{DF}$ for $W = Z/L$ one can solve Eq. 28 for l_{DF} at the snapping condition ($F=0$):

$$l_{DF} = \left(\frac{\sqrt{2a}AZ}{k_e} \right)^{2/7} \left[\frac{1}{36WR^2} \times \left(\frac{1}{[1-R]^{3/2}} - \frac{1}{\left[1 - \frac{R(1-W)^2(2+W)}{2}\right]^{3/2}} \right) \right]^{2/7}. \quad (29)$$

6.2 Comparison of the 1D SPF and 2D DF models

Fig. 7 presents an overall comparison of the probe bending error (or the total probe bending) for the 1D SPF (Eq. 5) and 2D DF (Eq. 29) models. The analytical DF model shows a meaningful solution for both limiting cases of $Z/L = 0$ and $Z/L = 1$. Like the numerical DF model (Section 5), the analytical DF model predicts a smaller bending error than the 1D SPF model (Fig. 7). The numerical DF model seems to underestimate the bending error (Fig. 7). This could be anticipated since numerical solution clearly shows underestimation of probe bending after the snapping condition ($F = 0$ and $dF/d\omega = 0$) is reached (Fig.5). It has to be noted that an accuracy of the analytical DF model is yet to be studied. Observed close (sub 0.1 nm) match between $\omega_{DF}(x)$ and $\omega_{SPF}(x)$ does not necessarily guarantee the required (sub 1 nm) accuracy of the l_{DF} calculation [20].

The new analytical DF model confirms (in agreement with numerical DF model) that the ratio of probe bending estimated using the simple 1D SPF model and the complex but accurate 2D DF model depends on Z/L ratio in a simple linear way (Fig. 7). Thus, the probe bending error can be accurately estimated using an expression:

$$l_{DF} \cong \frac{0.91}{(1+0.27\frac{Z}{L})} \times \left(\frac{\sqrt{a}AZ}{k_e}\right)^{2/7}. \quad (30)$$

Since usually $k_p \ll k_t$ so that $k_p \cong k_e$ (Eq. 7), one can further simplify Eq. 30 and express the probe bending error showing its dependencies on physical characteristics of the sample-probe system:

$$l_{DF} \cong \frac{0.71}{(1+0.27\frac{Z}{L})} \times \frac{1}{a} \times \left(\frac{AZL^3}{E}\right)^{2/7}. \quad (31)$$

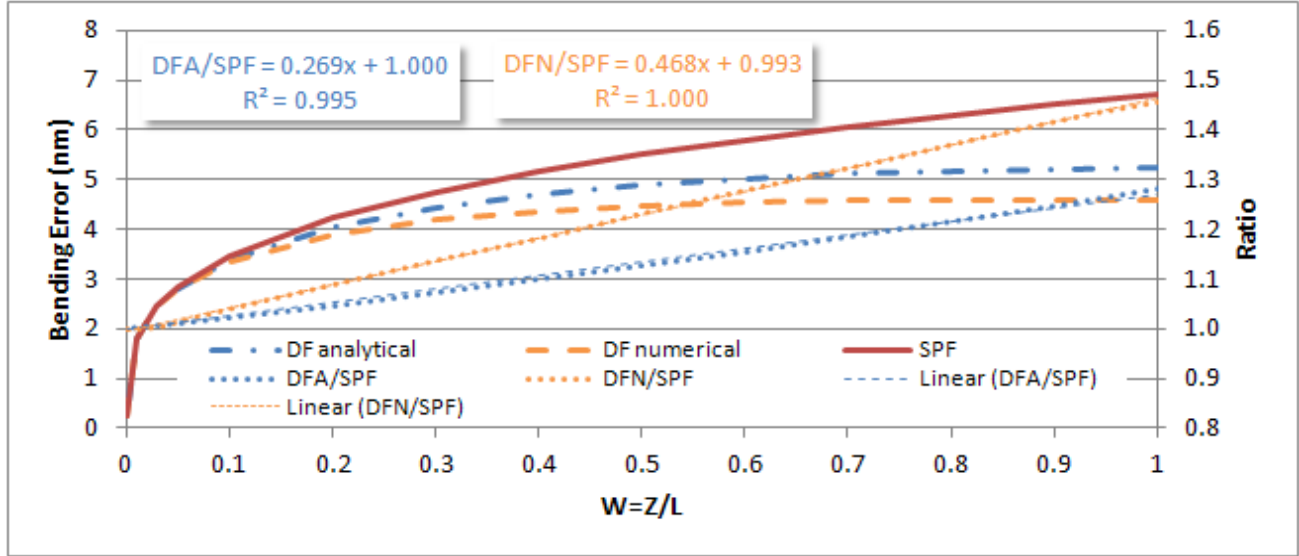


Figure 7. Comparison of probe bending error as a function of sidewall-probe overlap Z calculated using the 1D SPF and DF models for a 480 nm long CNT probe with $a = 15$ nm, $E = 0.5$ TPa, and $A = 3.95$ eV.

Equations 30 and 31 rather than Eq. 6 should be used for accurate extraction of fundamental sample-probe characteristics from experimental probe bending data (Section 4, Eq. 14). Probe bending modeling could be developed further by including probe misalignment. Preliminary (not presented in this paper) data indicate that for the 480 nm CNT probe (Fig. 7) misalignment of 1° (which is common for CNT probes) may cause an additional bending error of ≈ 1 nm. Development and testing of such a new model will take significant additional effort and is beyond the scope of this paper [20].

7. CONCLUSION

In this work we have developed and tested 1D SPF and 2D DF models of the CD-AFM bias related to the bending of cylindrical probes. An earlier model reported by Watanabe *et al.* [3] was refined. Contributions from several new phenomena were considered. The methodology for extraction of the Hamaker probe-surface interaction energy from experimental probe bending data was developed. In contrast with previously published results [3], the revised 1D SPF model and new data evaluation methodology yield significantly lower Hamaker energies of 1.5 eV to 6.1 eV.

The 1D SPF model was based on questionable assumptions about the probe-sample interaction. We checked the impact of these assumptions on the model accuracy through comparison of its results with an exact 2D numerical solution. A new 2D distributed force model was developed to describe the probe bending and snapping phenomena. Complications of numerical methods near the unstable probe snapping point were overcome using a so-called 2D single point

approximation. As a result of this investigation, a new analytical 2D DF model of probe bending and snapping was developed.

Comparison of this new model with the 1D SPF model revealed about a 27 % discrepancy in probe bending bias between the two. A simple linear relation between results of 1D SPF and 2D DF models was found. It is important to emphasize that the observed relation depends exclusively on the Z/L ratio. This finding would simplify the use of the advanced 2D DF model of probe bending in various CD-AFM applications. This work shows that cylindrical probe bending and the resultant error (edge detection bias) of CD-AFM can be quite significant – on the order of several nanometers. Therefore, modeling and correction of the bias is a necessary element of accurate CD-AFM metrology using cylindrical probes.

As an expansion of this work, we plan to develop bending models for probes with flared or other non-cylindrical geometries. Clarification of the differences in experimental data reported by various authors is needed. Improvements in AFM hardware and experimental methodology may also be necessary to answer existing questions. New 2D and 3D analysis methods for CD-AFM data should be created to take full advantage of the new bias correction modeling capabilities that we have developed in this work.

REFERENCES

- [1] Rana, N., et al., “Reconciling measurements in AFM reference metrology when using different probing techniques,” Proc. SPIE 7971, 7971-17 (2011).
- [2] Cordes, A., “Sidewall slope sensitivity of CD-AFM metrology,” Proc. SPIE 8105, 8105-05 (2011).
- [3] Watanabe, M., et al., “A Novel AFM Method for Sidewall Measurement of High-Aspect Ratio Patterns,” Proc. SPIE 6922, 69220J (2008).
- [4] Rajter, R.F., et al. “van der Waals-London dispersion interactions for optical anisotropic cylinders: metallic and semiconducting single-wall carbon nanotubes,” Phys. Rev. B 76, 045417 (2007).
- [5] McClure, P.F. and Mancevski, V., “Calibration of dual probe NanoCaliper™ AFM for CD metrology,” Proc. SPIE 5752, 922 (2005).
- [6] Visser, J., “Adhesion of colloidal particles,” [Surface and Colloid Science], vol. 89, NY, Academic Press (1976).
- [7] <http://www.team-nanotec.com/index.cfm>
- [8] Orji, N.G., et al., “Towards accurate feature shape metrology,” Proc. SPIE Vol. 6922, 692208 (2008).
- [9] Morimoto, T., et al., “New atomic force microscope method for critical dimension metrology,” Proc. SPIE 5038, 636-643 (2003).
- [10] <http://www.vlsistandards.com>
- [11] Akita, S., et al., “Influence of force acting on side face of carbon nanotube in atomic force microscopy,” Jpn. J. Appl. Phys., Vol. 39, 3724-3727 (2000).
- [12] Akita, S., et al., “Influence of stiffness of carbon-nanotube probes in atomic force microscopy,” J. Phys. D: Appl. Phys. Vol. 33, 2673-2677 (2000).
- [13] Private communication.
- [14] Tanigaki, T., et al., “Three-dimensional evaluation of an independent multi-walled carbon nanotube probe by tomography with high-resolution transmission electron microscope,” Journal of Electron Microscopy, Vol. 60, 19-24 (2011).
- [15] Timoshenko, S.P., [History of strength of materials], McGraw-Hill New-York (1953).
- [16] Gere, J.M. and Timoshenko, S.P., [Mechanics of Materials], PWS Publishing Company (1997).
- [17] Meyer, E., et al., “Comparative study of lithium fluoride and graphite by atomic force microscopy (AFM),” J. Microscopy, Vol. 151, 269 (1988).
- [18] Meyer, E., et al., “Atomic force microscopy for the study of tribology and adhesion,” Thin Solid Films, Vol. 181, 527 (1989).
- [19] Sarid, D., [Scanning Force Microscopy with applications to electric, magnetic and atomic forces], NY, Oxford, Oxford University Press, 212-215 (1994).
- [20] Observing the SPIE proceedings volume limitations we do not present detailed mathematical derivations here. The details will be published elsewhere.